AIAA 2002-1249

HUBBLE SPACE TELESCOPE POINTING PERFORMANCE DUE TO MICRO-DYNAMIC DISTURBANCES FROM THE NICMOS CRYOGENIC COOLER

Brian R. Clapp
Lockheed Martin Technical Operations, Greenbelt, MD USA
Brian.Clapp@lmco.com

Joel W. Sills Jr.
United Space Alliance, Houston, TX USA
Joel.W.Sills@USAHQ.UnitedSpaceAlliance.com

Carl R. Voorhees
Lockheed Martin Space Systems – Missiles and Space Operations, Newtown, PA USA
Carl.Voorhees@lmco.com

ABSTRACT

The Vibration Emittance Test (VET) was performed to measure the emitted disturbances of the Near Infrared Camera and Multi-Object Spectrometer (NICMOS) Cryogenic Cooler (NCC) in preparation for NCC installation onboard the Hubble Space Telescope (HST) during Servicing Mission 3B (SM3B). Details of the VET ground-test are described, including facility characteristics, sensor complement and configuration, NCC suspension, and background noise measurements. Kinematic equations used to compute NCC mass center displacements and accelerations from raw measurements are presented, and dynamic equations of motion for the NCC VET system are developed and verified using modal test data. A MIMO linear frequency-domain analysis method is used to compute NCC-induced loads and HST boresight jitter from VET measurements. These results are verified by a non-linear time-domain analysis approach using a high-fidelity structural dynamics and pointing control simulation for HST. NCC emitted acceleration levels not exceeding 35 micro-g rms were measured in the VET, and analysis methods herein predict 3.1 milli-arcseconds rms jitter for HST on-orbit. Because the NCC is predicted to become the predominant disturbance source for HST, VET results indicate that HST will continue to meet the 7 milli-arcsecond pointing stability mission requirement in the post-SM3B era.

INTRODUCTION

The purpose of this document is to describe details of the Vibration Emittance Test, define the analysis method used to compute NCC-induced disturbance loads, and predict Hubble Space Telescope on-orbit jitter due to the NCC. Four objectives of this work are listed in order of descending importance: 1) verify that HST will comply with the 7 milli-arcsecond pointing stability requirement after the installation of the NICMOS Cooling System (NCS) which includes the NCC, 2) quantify NCC-induced disturbances as measured in the VET, 3) characterize the spectral content of NCC emitted disturbances, and 4) assess structural dynamic coupling between NCC emitted disturbances and other HST structural modes.

Beyond application for HST, this work illustrates three items significant for structural dynamic analysis on other spacecraft programs. Methods are presented to quantify and characterize micro-dynamic disturbances (greater than 9 micro-g rms) in ground test over a broad frequency range (0.001 Hz – 50 Hz) for application to precision orbiting platforms. The emitted disturbances from one cryogenic cooling machine are characterized spectrally, revealing spectral content at integer multiples of the fundamental disturbance frequency. Finally, the NCC demonstrates new cryogenic cooling technology applicable to other infrared science space missions with stringent disturbance requirements.

HST BACKGROUND

The Hubble Space Telescope is the premiere observatory for astronomy in visible and infrared wavelengths. Unlike the other NASA Great Observatories, HST was designed to be serviced on-orbit, and therefore, HST functions as a high-precision optical platform for state-of-the-art science instruments during its 20-year mission. During routine operation, HST achieves pointing stability levels of 3 milli-arcseconds measured over 60-second rms intervals and thereby satisfies the 7 milli-arcsecond rms mission requirement.

During the Second Servicing Mission in 1997, the NICMOS instrument was installed onboard the observatory to expand HST science capabilities into the infrared spectrum. Soon thereafter, thermal monitoring of the instrument revealed that an unexpected heat load was depleting cryogen within the NICMOS internal dewar at a faster rate than planned. NICMOS science observations ceased in January 1999. Meanwhile, plans were underway within the HST program to develop a retrofit NICMOS Cooling System. The heart of the NCS is the NICMOS Cryogenic Cooler, a refrigeration machine designed to cool NICMOS detectors to revive the instrument for science operations. The NCS is planned for installation onboard the HST during SM3B in February 2002.

The HST Pointing Control Jitter Budget was amended in 1997 to accommodate new NCS disturbance sources. An additional 1 milli-arcsecond (mas) rms was allocated for the entire cooling system. The additional jitter error was assumed to be uncorrelated with existing HST jitter errors (3 mas rms). Combining these errors in Root-Sum-Square (RSS) fashion, HST jitter should not exceed 3.2 mas rms after cooling system installation, assuming cooling system components comply with the jitter budget. Of the 1 mas rms allocated for the cooling system, 0.77 mas rms was allocated for the NCC, as the cryogenic cooling pump was expected to be the predominant source of jitter from the NICMOS Cooling System.

Derived requirements for allowable accelerations at the NCC mass center were developed using the Pointing Control Jitter Budget, the HST attitude control law, and the HST post-SM3B structural dynamics model. RSS accelerations at the NCC mass center less than 4.1 micro-g rms (0.001 Hz – 50 Hz) are required to meet the 0.77 mas rms jitter budget allocation for the NCC. Assuming the entire 7 mas rms HST pointing stability requirement is due to NCC disturbances, the maximum allowable RSS acceleration at the NCC mass center is 38 micro-g rms over the same frequency range. These acceleration limits are approximate; they were used as guidelines during the VET to determine if measured NCC-induced accelerations were within acceptable HST jitter limits.

The HST boresight spectral sensitivity to disturbances at the NCC mounting location is illustrated in Figure 1. This disturbance rejection transfer function is a characteristic of the combined attitude control law and structural dynamic properties of the vehicle. The plot is typical of the twelve characteristic functions describing the HST attitude response due to force or torque loads applied at the NCC mass center. Figure 1 describes the HST pitch attitude response due to NCC X1-axis forces for the post-SM3B vehicle configuration. (The NCC VET coordinate frame is defined later.) The figure shows that low frequency force disturbances in the 0.01 Hz to 0.5 Hz range have the greatest affect upon HST boresight jitter. The resonant peaks above 0.4 Hz show evidence of the various structural modes of the HST and the fidelity of the structural dynamic models.

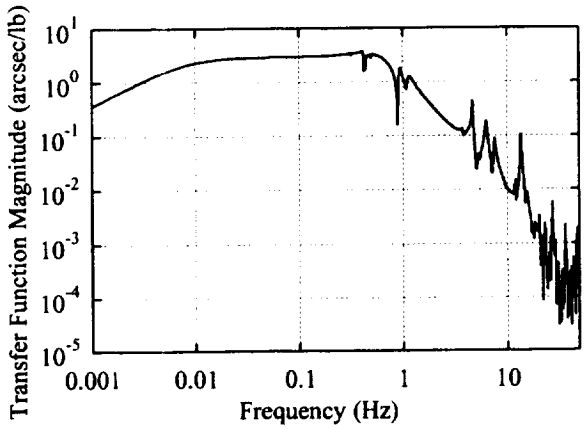

Figure 1. HST Closed Loop Disturbance Rejection Transfer Function from NCC X1 Force (lb) Input to HST Pitch Response (arcsec) Output

NCC BACKGROUND

The NICMOS Cryogenic Cooler is a refrigeration device using high-speed turbo-machines working on neon gas to cool NICMOS detectors to 73K. NCC internal components are mounted inside a metal frame measuring 26 inches long, 17 inches wide, 16 inches tall and weighing 217.5 lb, not including VET suspension fixtures. The NCC is treated as a single rigid body for analyses presented herein.

Disturbances within the NCC originate on the compression side of the refrigeration loop and are caused by pressure oscillations, or surging, at the output of the compressor. Surging occurs when NCC system temperatures are greater than 95K, and it is estimated that HST will be subject to NCC surging disturbances during the first 55 hours of NCS cooldown. At temperatures below 95K, surging disturbances diminish as steady-state flow ensues in the refrigeration loop; quantitative estimates for NCC emitted disturbances under steady state conditions are known, but high uncertainties accompany the results.[1]

The NCC compressor runs at speeds approaching 7500 rotations-per-second (rps), and surging disturbance acceleration levels increase with increasing shaft speed. Compared to the compressor, the circulator is a lower-power and lower-speed (1200 rps) turbo-machine within the NCC. The circulator was not run during the VET, as circulator disturbances are insignificant compared to compressor surging disturbances. Other documents describe additional details of the NCS and NCC operation.[2]

PREVIOUS DISTURBANCE MEASUREMENTS

An extensive testing program at NASA Goddard Space Flight Center began in 1997 to verify HST compliance with the 7 mas rms jitter requirement due to disturbances produced by the NCC and other sources. Ground testing and analysis of other hardware planned for installation during SM3B indicate the NCC is the predominant jitter-producing disturbance source.

Emitted disturbances from the NCC were measured during thermal-vacuum (TVAC) testing in preparation for the Hubble Orbital System Test (HOST), a payload onboard STS-95 containing components of the NCS. NCC surging and steady-state disturbances were measured during TVAC testing and HOST, producing a significant qualitative result: HST jitter due to surging disturbances is always greater than jitter due to steady-state disturbances.[1] Quantitative results were accompanied by high uncertainties due to random and systematic errors inherent to the test design. HST on-orbit jitter predictions, with uncertainties, from the HOST measurements were 4.5 mas rms during NCC steady-state operation and 27 mas rms during surging. The steady-state prediction exceeded the 0.77 mas rms requirement for the NCC and much of the 7 mas rms HST jitter requirement; the surging prediction violated all requirements. The HST project then approved a final ground test to quantify NCC-induced disturbances with low uncertainty and high confidence.

NCC VIBRATION EMITTANCE TEST

The Vibration Emittance Test was the culmination of the ground and on-orbit testing program for the NCC. The purpose of the VET was to quantify HST jitter due to NCC surging disturbances with no more than 25% uncertainty and 95% confidence. Accurately measuring surging disturbances and using the measurements to predict HST jitter provides an upper-bound jitter estimate for all modes of NCC operation, according to HOST results.

Five requirements for the VET were motivated by lessons learned from HOST/TVAC testing to reduce uncertainties and increase confidence in results: 1) use a low frequency suspension system to reduce mechanical grounding and mass participation systematic errors, 2) select a facility with low background noise relative to HST requirements, 3) increase ensemble length to 1000 seconds to resolve low frequency disturbances down to 0.001 Hz, 4) acquire at least 64 ensembles to reduce random errors to 25% or less with 95% confidence, and 5) select sensors to measure both rotational and translational disturbances. Three additional requirements were added that were unique to the VET: 1) characterize VET system dynamics so that forces below the suspension frequency may be computed, 2) run the NCC compressor at two speeds to characterize surging disturbances as a function of speed, and 3) monitor acceleration levels during the VET for compliance with derived requirement levels (RSS acceleration less than 38 micro-g rms to meet the 7 mas rms HST jitter requirement, and 4.1 micro-g rms to meet the 0.77 mas rms NCC jitter requirement).

The requirements for background noise and ensemble length affected other aspects of the VET. The background noise requirement eliminated TVAC facilities from consideration. A test at ambient temperatures implied testing only NCC surging operation, as NCC steady-state operation cannot be achieved in ambient conditions. Therefore, the background noise requirement eliminated the possibility of measuring steady-state disturbances in the VET. The 1000-second ensemble length restricted compressor speeds to 6500 rps or lower due to NCC thermal concerns at ambient temperatures. The compressor was run at 6500 rps during several tests, but

the majority of tests were run at 5800 rps to prevent damage to NCC components.

INSTRUMENTATION AND DATA ACQUISITION

Twelve Honeywell QA-2000 Servo Accelerometers and six Kaman eddy current displacement probes were the primary sensors used for VET disturbance measurements. The servo accelerometers were selected because of their potential for sensing low g-levels and low-frequency vibration.[3] The servo accelerometers were mounted in aluminum cubes in clusters of four, and attached to the NCC as shown in Figure 2. Three servo accelerometer quads were mounted on three faces

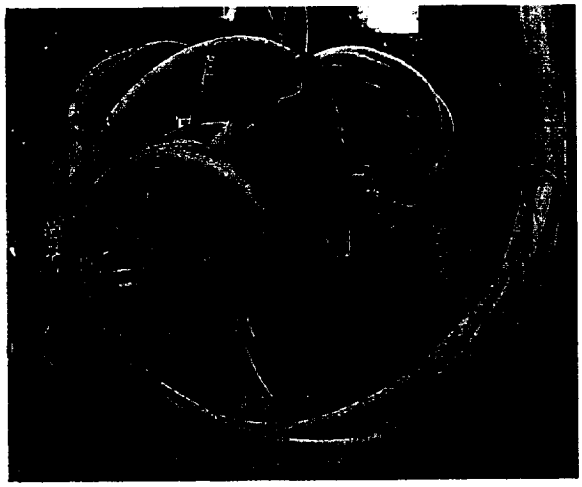

Figure 2. Honeywell QA-2000 Servo Accelerometer Quad

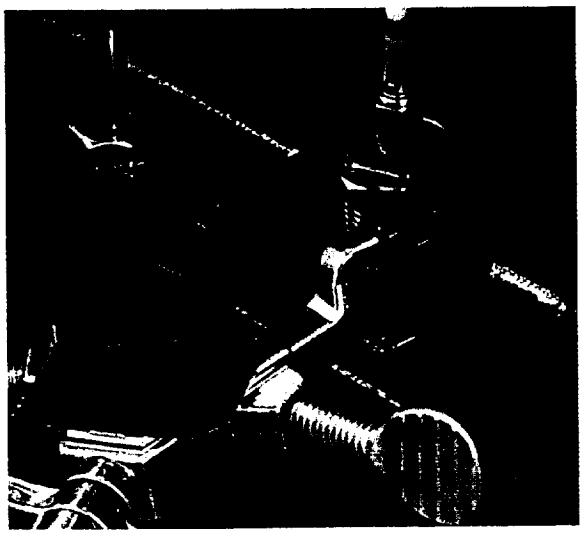

Figure 3. Kaman Eddy Current Displacement Probe

of the NCC to measure six degrees-of-freedom motion of the suspended machine. By mounting the accelerometers back-to-back, two independent measurements of each component of acceleration were acquired, thereby collecting two independent ensembles per test run. This technique was chosen to reduce the number of overall tests run without increasing random errors.

Eddy current probes were used to measure rigid-body displacements of the suspended NCC. The probes were mounted on test stands to measure displacements relative to the facility floor, as shown in Figure 3. The objective of the displacement measurement was to resolve low-frequency forces below VET suspension frequencies. Eddy probe data was also used for modal data processing.

Data from these and other sensors were acquired by the Pacific Instruments 6000 data acquisition system. One feature of the PI6000 allowed each accelerometer data channel to be acquired by two acquisition channels, set for different input scaling. This was done to achieve a large dynamic range of acceleration measurement. Previous disturbance measurements from the HOST mission, although corrupted by high background noise, indicated that peak NCC accelerations could approach 30 milli-g. At the low end of the dynamic range, measurement of 4.1 micro-g rms or less was required to verify compliance with the 0.77 mas rms NCC jitter allocation. Setting the minimum-bit amplitude in the nano-g range ensured a small-amplitude measurement capability if the NCC was quieter than HOST measurements indicated.

TEST FACILITY

The testing was conducted in a large Reverberant Acoustic Test Facility (RATF), located at the facilities of the Lockheed Martin Space Systems Communications and Power Center in Newtown, Pennsylvania, between July 9-27, 2000. The RATF is a 60K cubic-foot chamber that is used mainly for high-intensity acoustic noise testing. Its dimensions are 30 ft by 50 ft by 40 ft high, with 18-inch heavily reinforced concrete walls, a large 25 ft by 40 ft high rolling concrete specimen door, man-door, and 5-ton bridge crane. Six horns are mounted in the ceiling and are capable of generating sound pressure levels up to 155 dB. The floor and foundation of the chamber are quite substantial, just to support the weight of the facility, and are mechanically isolated from the surrounding building. The chamber sits on a prepared soil and sand

foundation, as its only other isolation. As such, the combination of mass and isolation provide for an extremely quiet ambient background noise environment inside the chamber.

An ambient lateral measurement on the floor of the RATF was performed using the servo accelerometers, and the autospectral density function using 40 spectral averages is shown in Figure 4. The lateral acceleration is 3.9 micro-g rms (0.001 Hz – 20 Hz). The RSS acceleration of this component with the other two measured components yields 8.9 micro-g rms (0.001 Hz – 50 Hz). Onboard HST, if the NCC emits disturbances at this level, the resulting boresight jitter will be 1.7 mas rms. This fact illustrates the unprecedented pointing stability of the Hubble Space Telescope and the stringent disturbance requirements expected for HST components.

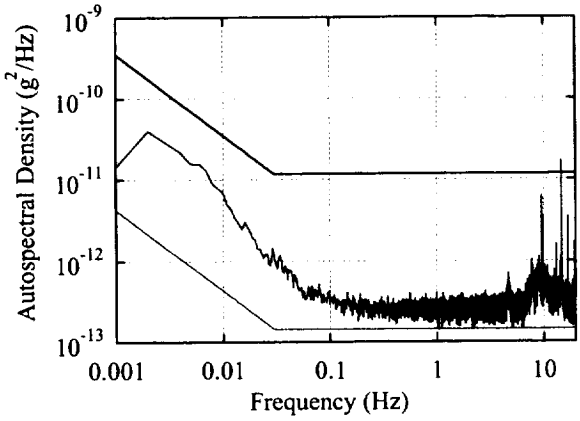

Figure 4. RATF Floor Noise Lateral Acceleration Autospectrum (brown) and Derived Requirement Acceleration Autospectra for 7 mas rms (black) and 0.77 mas rms (purple) HST Jitter Levels

The black curve in Figure 4 shows the autospectral density of the derived acceleration requirement at the NCC mass center at the 7 mas rms HST jitter level. This curve is the autospectrum for a single component of acceleration. If all three components of acceleration have this autospectra, they act together at the NCC mass center to produce 7 mas rms of HST jitter. Similarly, the purple curve shows the derived acceleration requirement at 0.77 mas rms HST jitter. All VET measurements exceed the 0.77 mas rms NCC requirement, because the floor noise exceeds the requirement. RATF floor noise is well below the 7 mas rms HST pointing stability requirement, demonstrating why this facility and these sensors were selected for the VET project.

TEST CONFIGURATION

The NCC was suspended from the ceiling of the RATF using three 28-foot kevlar cords to achieve a low-frequency lateral suspension approaching 0.17 Hz, as shown in Figures 5 and 6. Suspending the NCC in this manner achieves a low-frequency suspension for VET X1-axis and X2-axis translations and X3-axis rotation. The kevlar cords were attached to three pneumatic suspension devices (Figure 7), or "Anti-Gravity Machines" (AGMs), that isolated the payload from the test support structure installed at the RATF ceiling.

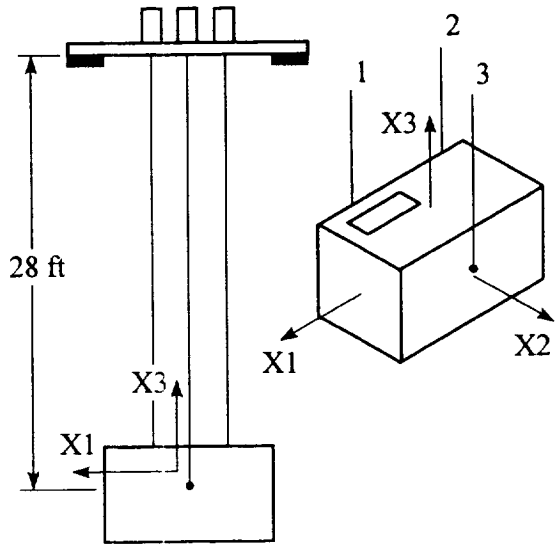

Figure 5. Sketch of VET Configuration A

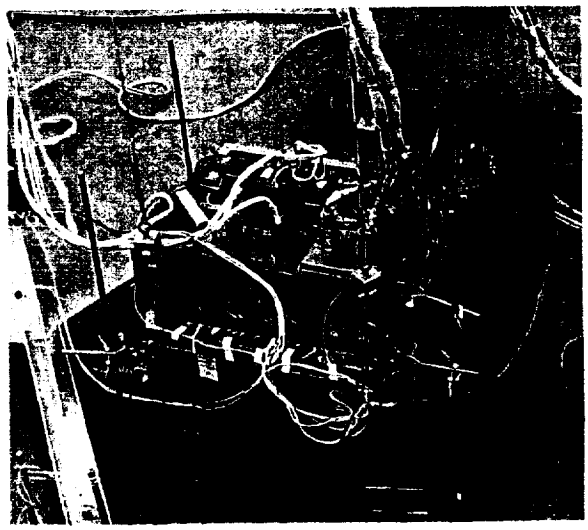

Figure 6. NCC Suspended during the VET

The AGMs, acting independently, provide a low-frequency suspension for VET X1-axis and X2-axis rotations and X3-axis vertical translation.[4] Facility nitrogen gas was regulated and used to pressurize the AGMs.

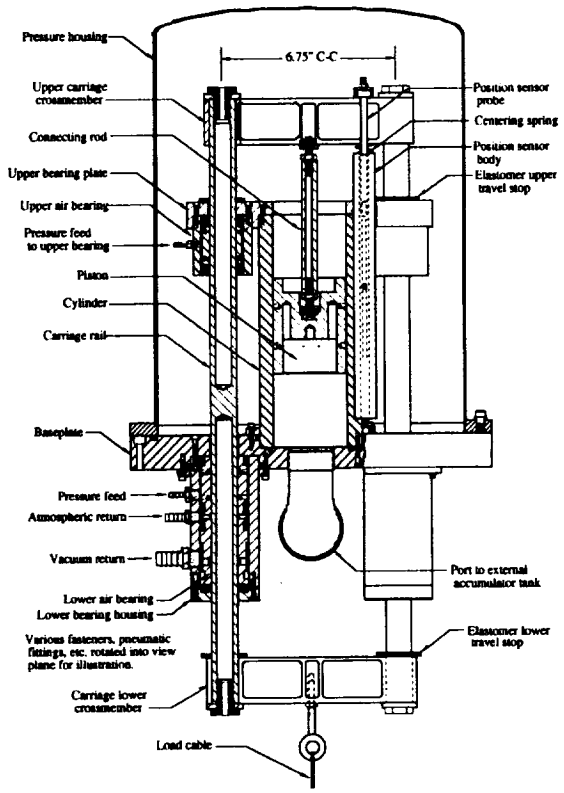

Figure 7. Pneumatic Suspension Device, or "Anti-Gravity Machine" (AGM)

Prior to running the NCC, background noise measurements were performed for spectral characterization of the VET suspension system. Autospectral densities of these measurements are shown in the following two figures. Figure 8 shows the lateral X1-axis background noise using 6 spectral averages for AGMs on and 80 spectral averages for AGMs off. This plot shows that the lateral background noise was much greater with the AGMs on, and consequently, the test team decided to run the VET with the AGMs off, or unpressurized. With the AGMs unpressurized, the carriage (Figure 7) rests on elastomeric pads against the body of the AGM. If the AGMs had been used during the VET, the background noise alone would have exceeded the 7 mas rms HST jitter requirement. Figure 9 is a similar plot for the vertical X3-axis background acceleration. A similar result is observed for this component of acceleration: the AGMs introduce low-frequency noise below 0.6 Hz. Although only six spectral averages are used to compute the acceleration autospectrum with the AGMs on, Figure 9 shows that the AGMs provide good vertical isolation of the payload above 0.6 Hz. This illustrates the benefits of using AGMs for other applications.

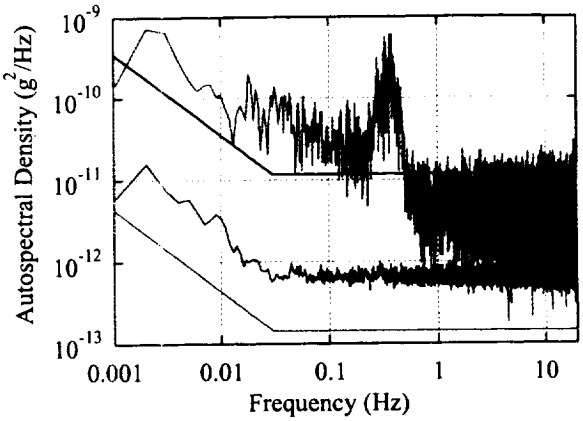

Figure 8. VET X1-axis Background NCC Mass Center Acceleration Autospectra for NCC Off and AGMs On (green) and AGMs Off (red). Derived Requirement Acceleration Autospectra for 7 mas rms (black) and 0.77 mas rms (purple) HST Jitter Levels

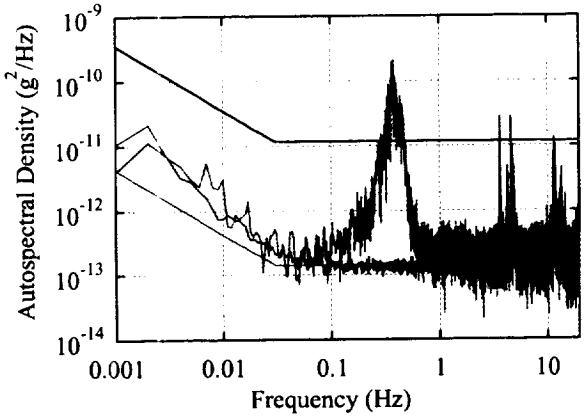

Figure 9. VET X3-axis Background NCC Mass Center Acceleration Autospectra for NCC Off and AGMs On (green) and AGMs Off (red). Derived Requirement Acceleration Autospectra for 7 mas rms (black) and 0.77 mas rms (purple) HST Jitter Levels

The strategy for suspending the NCC changed after the decision to turn-off the AGMs. With the AGMs off, only three degrees-of-freedom of the NCC benefited from the low-frequency pendulum suspension (X1 and X2 translation and X3 rotation), so the VET team decided to re-orient the NCC mid-way through the test

to Configuration B, shown in Figure 10. In this configuration, dynamic motion in X3-translation and X2-rotation were also given a low-frequency suspension. A third orientation of the NCC was proposed to measure dynamics of the X1-rotation degree-of-freedom, but operational limitations of the NCC prevented this. Using two configurations during the VET, disturbances were measured using a low-frequency suspension for five-of-six rigid-body degrees-of-freedom of the NCC.

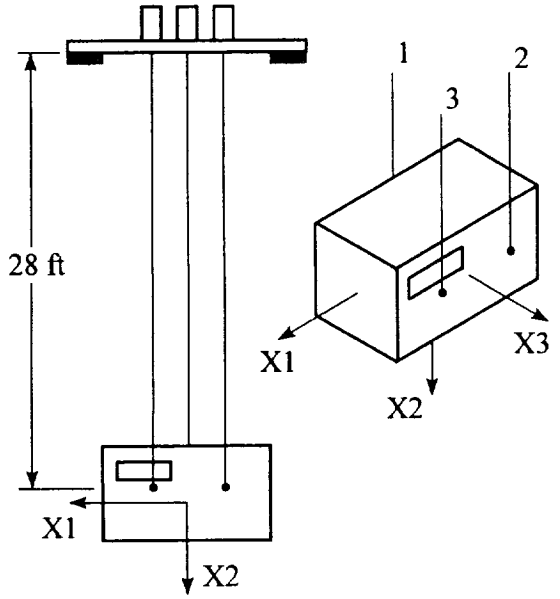

Figure 10. Sketch of VET Configuration B

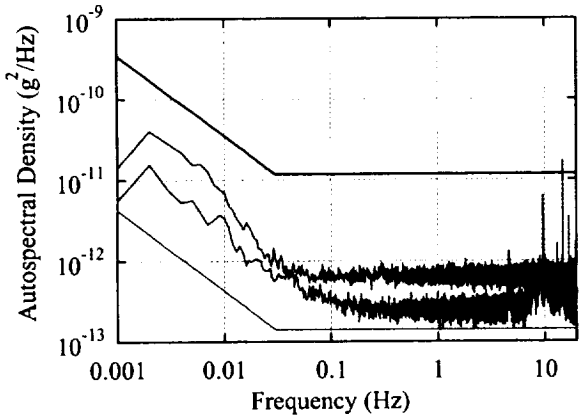

Figure 11. VET X1-axis Background NCC Mass Center Acceleration Autospectra for NCC Off and AGMs Off (red). RATF Floor Noise Lateral Acceleration Autospectrum (brown) in X1-axis Direction. Derived Requirement Acceleration Autospectra for 7 mas rms (black) and 0.77 mas rms (purple) HST Jitter Levels

The RATF floor lateral background noise and the suspended NCC (in Configuration A with AGMs off) X1-axis background noise are shown in Figure 11. A comparison of background noise levels shows that the suspended NCC has a higher noise floor above 0.04 Hz, but a lower noise floor below that frequency. The RATF noise floor curve is the same data described in Figure 4 with an RSS acceleration of 8.9 micro-g rms (0.001 Hz – 50 Hz). The suspended NCC autospectrum was computed using 80 spectral averages, and this single component of acceleration is 5.1 micro-g rms (0.001 Hz – 20 Hz). The RSS acceleration of this component with the other two measured components yields 20 micro-g rms. Onboard HST, if the NCC emits disturbances at this level, the resulting boresight jitter will be 3.2 mas rms. With the NCC suspended and AGMs off, the background noise was within acceptable levels to achieve test goals, and the test team proceeded with the VET.

SENSOR DATA PROCESSING AND KINEMATICS

The sensor distribution for the eddy current displacement probes and servo accelerometers are shown in Figures 12 and13, respectively.

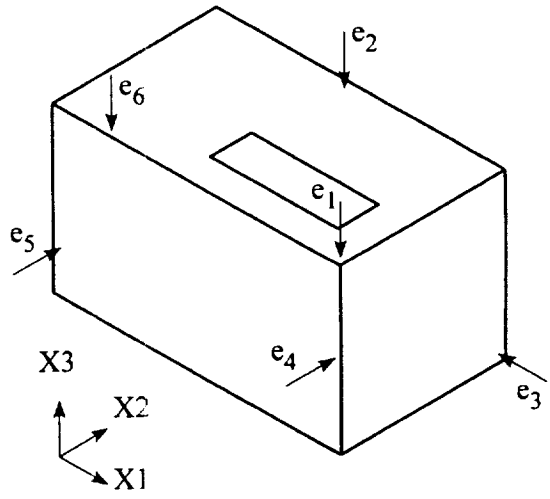

Figure 12. VET Eddy Probe Distribution

Prior to transforming servo acceleration measurements from sensor frame to the VET mass center frame, the acceleration measurements were corrected for bias and scale factor as a function of temperature according to guidelines from the manufacturer. Each QA-2000 accelerometer contains an internal temperature sensor, and servo temperatures were acquired with the PI6000.

External heat generated by the NCC in cooling the neon working fluid caused servo accelerometer temperatures to increase by as much as 8° C during each 1000-second test.

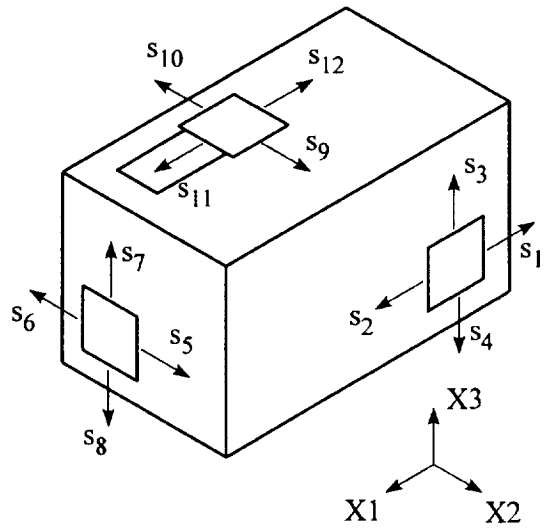

Figure 13. VET Servo Accelerometer Distribution

Kinematic equations transforming eddy probe displacements and servo accelerometer measurements from sensor frame to VET mass center frame are shown in Equations (1) and (2), respectively. The transformation tensors are functions of sensor orientations and locations with respect to the VET mass center.

$$e_i = E_{ij} y_j \qquad i,j = 1,2,\ldots 6 \tag{1}$$

e_i Displacement measurement

y_j VET mass center translation and rotation states

E_{ij} Displacement transformation tensor from eddy probe i to VET mass center component j

$$\begin{aligned} s^1_{2i-1} &= S^1_{ij}\ddot{y}_j \qquad i,j = 1,2,\ldots 6 \\ s^2_{2i} &= S^2_{ij}\ddot{y}_j \qquad i,j = 1,2,\ldots 6 \end{aligned} \tag{2}$$

s^k_i Acceleration measurement for sensor set k

S^k_{ij} Acceleration transformation tensor from accelerometer i to VET mass center component j for sensor set k

Accelerometers are divided into two sets (even and odd sensors) for processing, which produces two independent acceleration measurements per test run. The linear accelerometer transformation equations assume the products of NCC body rates are insignificant; this was verified during post-test analysis. Generally, the acceleration transformation tensor, S, is a time variant tensor, as it depends upon NCC rotations over time relative to the static NCC position. NCC rotations were small, resulting in no loss of accuracy to use a time invariant tensor for VET post-processing. VET mass center displacements and accelerations are computed from sensor measurements by inverting Equations (1) and (2), as shown in Equations (3) and (4). The VET mass center was slightly offset from the NCC mass center, so computation of NCC mass center displacements and accelerations requires another transformation of the output from Equations (3) and (4) that affects only rotational states.

$$y_j = E^{-1}_{ij} e_i \qquad i,j = 1,2,\ldots 6 \tag{3}$$

$$\begin{aligned} \ddot{y}^1_j &= \left(S^1_{ij}\right)^{-1} s^1_{2i-1} \qquad i,j = 1,2,\ldots 6 \\ \ddot{y}^2_j &= \left(S^2_{ij}\right)^{-1} s^2_{2i} \qquad i,j = 1,2,\ldots 6 \end{aligned} \tag{4}$$

VET SYSTEM DYNAMIC CHARACTERISTICS

The single rigid body equations of motion for the NCC VET system for Configuration A are shown in Equation (5). A companion set was also constructed for VET Configuration B. The mass, damping and stiffness matrices are functions of five sets of parameters: 1) NCC external wire harness damping and stiffness, 2) Kevlar suspension cord axial damping and stiffness, 3) cord eyehook locations with respect to the VET system mass center, 4) suspension cord length, and 5) cord tension forces.

$$M^A_{ij}\ddot{y}_j + C^A_{ij}\dot{y}_j + K^A_{ij} y_j = F_i \qquad i,j = 1,2,\ldots 6 \tag{5}$$

F_i NCC emitted forces and torques at VET mass center

VET system dynamic equations for NCC emitted load inputs and VET mass center displacement and acceleration outputs are shown in Equations (6) and (7). For simplicity, the designation of VET configurations was omitted.

$$\begin{aligned} \dot{x}_i &= A_{ij} x_j + B_{ik} u_k \qquad i,j,l = 1,2,\ldots 12 \\ z_l &= C_{lj} x_j + D_{lk} u_k \qquad k = 1,2,\ldots 6 \end{aligned} \tag{6}$$

$$A_{ij} = \begin{bmatrix} 0 & \delta_{\alpha\beta} \\ -M^{-1}_{\alpha\beta}K_{\beta\gamma} & -M^{-1}_{\alpha\beta}C_{\beta\gamma} \end{bmatrix} \quad B_{ik} = \begin{bmatrix} 0 \\ M^{-1}_{\alpha\beta} \end{bmatrix}$$

$$C_{lj} = \begin{bmatrix} \delta_{\alpha\beta} & 0 \\ -M^{-1}_{\alpha\beta}K_{\beta\gamma} & -M^{-1}_{\alpha\beta}C_{\beta\gamma} \end{bmatrix} \quad D_{ik} = \begin{bmatrix} 0 \\ M^{-1}_{\alpha\beta} \end{bmatrix} \quad (7)$$

$$x_j = \begin{bmatrix} y_\alpha \\ \dot{y}_\alpha \end{bmatrix} \quad z_l = \begin{bmatrix} y_\alpha \\ \ddot{y}_\alpha \end{bmatrix} \qquad i,j,l = 1,2,\ldots 12$$

$$u_k = \begin{bmatrix} F_\beta \end{bmatrix} \qquad \alpha,\beta,\gamma,k = 1,2,\ldots 6$$

Modal testing was performed on the VET system for both configurations using a Kistler 9722A500 load cell hammer with a 1-inch gray silicon rubber tip and no extender mass. A 1-inch thick foam pad was taped to the NCC as a hammer target (see Figure 14) to lengthen the duration of the input impulse. Numerous load application points were chosen to excite the six rigid-body degrees-of-freedom of the VET system to characterize NCC suspension dynamics.

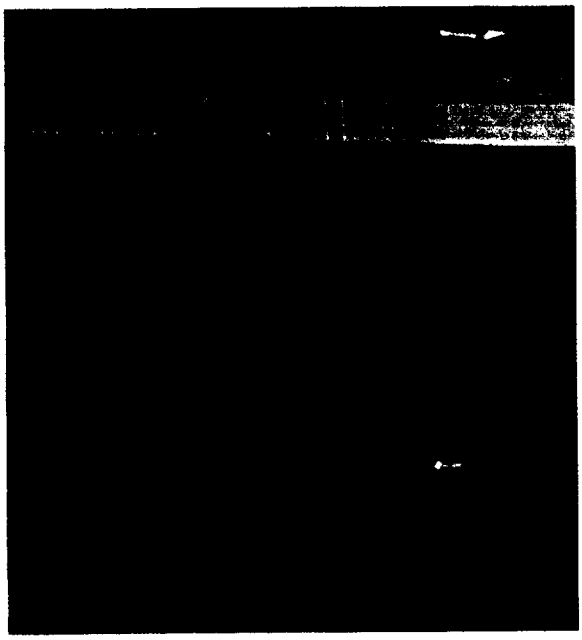

Figure 14. VET Modal Testing

The modal testing equations of motion for hammer tap inputs and eddy probe and servo accelerometer sensor outputs are shown in Equations (8) and (9). They were derived from Equations (1), (2), (6), and (7). Time and frequency domain methods were used to tune these equations to match modal test data, validating the VET system dynamic model. For example, Figure 15 shows an overlay time response for Eddy Probe #6, measuring X3-axis lateral response for VET Configuration B. The red curve shows the experimental measurement, and the blue curve is the simulated time response of Equation (8), driven by the measured hammer load time history.

$$\begin{aligned} \dot{x}_i &= A_{ij}x_j + B_{ik}L_{km}u^h_m \qquad i,j,l = 1,2,\ldots 12 \\ z^h_n &= J_{nl}C_{lj}x_j + J_{nl}D_{ik}L_{km}u^h_m \qquad k,m = 1,2,\ldots 6 \\ & \qquad\qquad\qquad\qquad\quad n = 1,2,\ldots 18 \end{aligned} \quad (8)$$

$$J_{nl} = \begin{bmatrix} E_{\alpha\beta} & 0 \\ 0 & S^1_{\alpha\beta} \\ 0 & S^2_{\alpha\beta} \end{bmatrix} \quad z^h_n = \begin{bmatrix} e_\alpha \\ s^1_{2\alpha-1} \\ s^2_{2\alpha} \end{bmatrix} \quad \begin{aligned} &\alpha,\beta = 1,2,\ldots 6 \\ &l = 1,2,\ldots 12 \\ &n = 1,2,\ldots 18 \end{aligned} \quad (9)$$

u^h_m Hammer tap force at location m

L_{km} Transformation from hammer load m to VET mass center load k

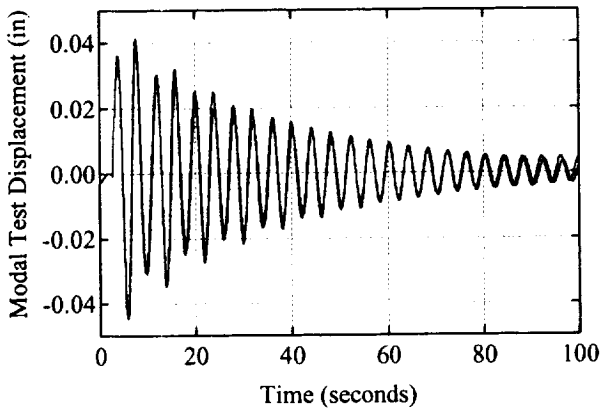

Figure 15. Modal Test Time Response (red) and Simulated Time Response (blue) due to Hammer Impulse Load for VET Configuration B Eddy Probe #6 Measurement

Modal parameters derived from the validated system dynamic models for VET Configurations A and B are shown in Tables 1 and 2, respectively. The lateral suspension frequencies were slightly higher than expected for a 28-foot pendulum system, and the cause is the external NCC wire harness bundles, shown in Figure 6. Inspection of the system dynamic equations of motion, Equation (5), shows that the wire harness stiffness acts in parallel with the pendulum "stiffness" to raise the system natural frequencies slightly. The wire harness stiffnesses for VET Configuration A were 0.39 lb/in X1-translation, 0.86 lb/in X2-translation and 247 in-lb X3-rotation. Configuration B stiffnesses were

0.44 lb/in X1-translation, 0.84 lb/in X3-translation and 245 in-lb X2-rotation.

Mode Description	Frequency (Hz)	Damping
X1 Pendulum	0.21	0.010
X2 Pendulum	0.25	0.020
X3 Torsion Pendulum	0.41	0.025
Cable #1 Axial Stretch	3.1	0.009
Cable #2 Axial Stretch	3.6	0.010
Cable #3 Axial Stretch	6.4	0.019

Table 1. VET Modal Parameters for Configuration A

Mode Description	Frequency (Hz)	Damping
X1 Pendulum	0.21	0.010
X3 Pendulum	0.25	0.017
X2 Torsion Pendulum	0.37	0.026
Cable #3 Axial Stretch	2.8	0.014
Cable #1 Axial Stretch	3.5	0.018
Cable #2 Axial Stretch	5.9	0.029

Table 2. VET Modal Parameters for Configuration B

The concepts used for quantifying NCC emitted disturbances from VET measurements are described using acceleration-to-force and displacement-to-force transfer functions derived from Equation (6). A transfer function for X1-axis acceleration input to X1-axis force output is shown in Figure 16 for VET Configuration A. This function shows that NCC emitted disturbance forces are proportional to acceleration measurements above the suspension frequency (0.21 Hz). The constant of proportionality is the VET system mass. This relationship illustrates the main reason for using a low-frequency suspension system during the VET: accelerometers can be used to measure force above the suspension frequency. Below the suspension frequency, accelerometers poorly measure force, as the figure illustrates. A transfer function for X1-axis displacement input to X1-axis force output is shown in Figure 17. This function shows that the suspension stiffness is the constant of proportionality between measured displacement and NCC emitted force below the suspension frequency. Therefore, displacement sensors are used to measure NCC emitted force below the suspension frequency, and accelerometers are used to measure NCC emitted force above the suspension frequency.

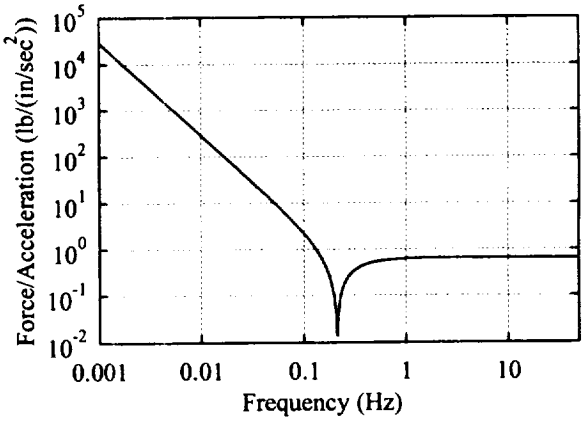

Figure 16. VET Configuration A Transfer Function for X1-axis Acceleration Input to X1-axis Force Output

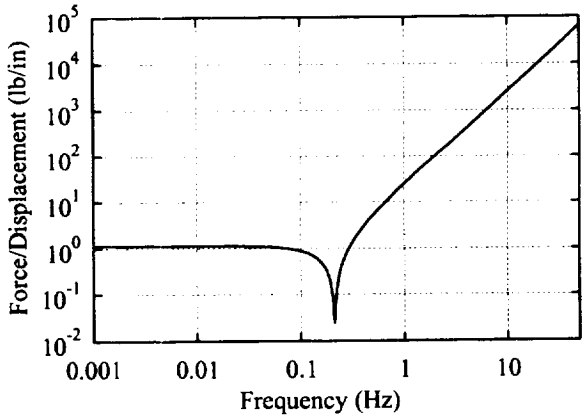

Figure 17. VET Configuration A Transfer Function for X1-axis Displacement Input to X1-axis Force Output

TEST RESULTS

Extraneous noise sources were minimized by restricting activity within the RATF during the VET. Only the NCC and the PI6000 data acquisition system were inside the chamber during test. The NCC command

and monitoring system was located outside the RATF, and wire harness cables were routed through a small feed in the chamber wall. Prior to beginning each test, the RATF specimen door was closed and the pneumatic seals were pressurized, the lights were turned-off, and the man-door was closed by the test conductor after starting the data acquisition system. Data acquisition was started when the NCC operator signaled that the compressor was at the correct speed. Data acquisition lasted 17 minutes (1020 seconds) for each test. The NCC compressor was then shut-down, and a portable air conditioning unit was turned-on to blow cool air directly at the NCC to cool its outer surfaces in preparation for the next test. Forty-three tests were run: four tests with the compressor running at 6500 rps and 26-tests at 5800 rps in Configuration A, and two tests with the compressor at 6500 rps and 11-tests at 5800 rps in Configuration B.

With the NCC running at 5800 rps, NCC emitted disturbance accelerations were higher than the VET noise floor but lower than the 7 mas rms HST jitter level, as Figure 18 indicates. The autospectrum was computed using 30 spectral averages from data acquired in Configuration A, and this single component of acceleration is 13 micro-g rms (0.001 Hz – 20 Hz). The RSS acceleration of this component with the other two measured components yields 34 micro-g rms, less than the 38 micro-g rms derived acceleration requirement. Onboard HST, if the NCC emits disturbances at this level, the resulting boresight jitter will be 3.6 mas rms, exceeding the NCC requirement but within HST mission limits.

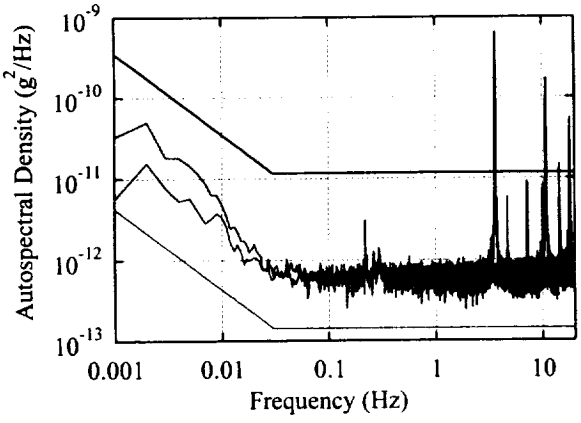

Figure 18. VET X1-axis NCC Mass Center Acceleration Autospectra for NCC Compressor at 5800 rps (blue) and NCC Off (red). Derived Requirement Acceleration Autospectra for 7 mas rms (black) and 0.77 mas rms (purple) HST Jitter Levels

Several spectral characteristics of NCC surging disturbances are evident by comparing the autospectra shown in Figure 18. The fundamental surging frequency is 3.5 Hz; surging also produces dynamic response at integer multiples of the fundamental frequency. An increase in dynamic response is evident at the VET suspension frequency of 0.21 Hz, but this does not imply large surging disturbances at this frequency. Rather, it reveals a characteristic of the VET system dynamics that amplifies acceleration responses to disturbance inputs at the VET suspension frequency. The transfer function reciprocal of Figure 16, a force-input to acceleration-output transfer function, shows this effect. NCC surging accelerations also rise above the noise floor at frequencies below 0.01 Hz, suggesting a low-frequency disturbance characteristic. Because disturbance forces are not proportional to acceleration below the suspension frequency, as discussed earlier, no conclusions will be made in this regard based upon acceleration measurement. However, displacement measurements also reveal evidence of low-frequency NCC disturbances.

Spectral characteristics of VET displacement measurements support the observations made using acceleration measurements. For VET Configuration A, Figure 19 shows the X1-axis displacement autospectra for the NCC off and NCC on.

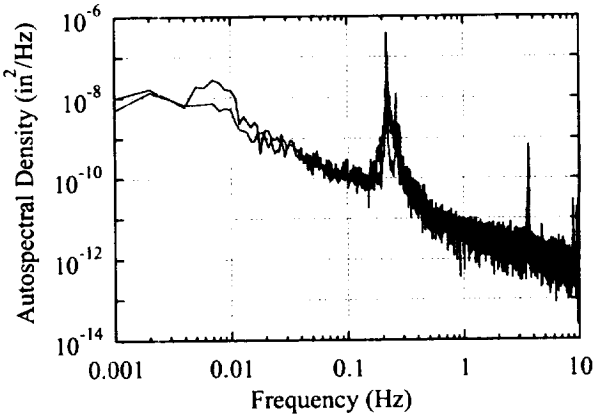

Figure 19. VET X1-axis NCC Mass Center Displacement Autospectra for NCC Compressor at 5800 rps (blue) and NCC Off (red).

The displacement background noise was computed using 15 spectral averages, and 5 spectral averages were used to compute the autospectrum with the NCC running. Again, the surging fundamental frequency rises above the noise floor at 3.5 Hz. The displacement response is amplified at the VET suspension frequency,

but the increased response is not due to large surging disturbances. The VET system amplifies displacement responses due to disturbance inputs at the suspension frequency, as indicated by the transfer function reciprocal of Figure 17. The displacement measurement supports the evidence of low-frequency surging disturbances below 0.01 Hz observed in acceleration data. The blue curve in Figure 19 rises above the noise floor between 0.004 Hz and 0.02 Hz, indicating the presence of NCC surging disturbances with periods ranging from 50 seconds to 4.2 minutes in duration. NCC disturbance forces are computed by combining displacement and accelerometer measurements as described in the next section.

The Vibration Emittance Test achieved the goal of measuring dynamic responses due to NCC-induced disturbances above the VET noise floor and below the 7 mas rms HST pointing stability requirement. Acceleration and displacement measurements were acquired and VET system dynamics were characterized to allow computation of emitted NCC surging disturbances and prediction of HST jitter. All VET requirements were met except one. The requirement to acquire 32 ensembles (yielding 64 acceleration ensembles using back-to-back sensors) was not achieved for each VET configuration; this was a consequence of the decision to run the VET using two NCC orientations.

COMPUTATION OF NCC EMITTED DISTURBANCES AND HST PERFORMANCE PREDICTIONS

Two methods are described and used in this section to predict HST on-orbit jitter due to disturbance forces and torques emitted by the NCC as measured in the Vibration Emittance Test. A linear frequency-domain analysis approach is described first, and a non-linear time-domain approach follows. The linear analysis method is more complex, but it is performed first to establish an algorithm to compute NCC emitted disturbances, thereby simplifying the steps required for the time-domain analysis. The non-linear analysis method uses the HST Pointing Control System time-domain simulation, HSTSIM, for high-fidelity predictions of HST on-orbit performance.

LINEAR FREQUENCY-DOMAIN ANALYSIS

The linear analysis method is a Multi-Input Multi-Output (MIMO) spectral analysis[5] approach that uses a linear representation of the HST attitude control law and a linear HST structural dynamics model in the post-SM3B configuration. The structural dynamic model was generated from the HST on-orbit finite element model.

VET mass center one-sided displacement spectral density functions are computed using Equation (10) after first blocking $y_i(t)$ from Equation (3) into n blocks of length $N\Delta t$ and averaging using n ensembles. The sample period for $y_i(t)$ is Δt, and N is the number of spectral values in the Fast Fourier Transform (FFT). This equation is written for VET Configuration A, and a companion equation can also be written for Configuration B.

$$\mathbf{D}^A_{ij}(f_k) = \frac{2}{nN\Delta t}\sum_{l=1}^{n} d^*_{il}(f_k)\, d_{jl}(f_k) \qquad i,j = 1,2,\ldots 6 \quad k = 0,1,\ldots \frac{N}{2} \tag{10}$$

$d_{il}(f_k)$ FFT of $y_i(t)$, block l, at frequency f_k

$d^*_{il}(f_k)$ Complex conjugate of $d_{il}(f_k)$

VET mass center one-sided acceleration spectral density functions for VET Configuration A are computed using Equation (11) after first blocking both sets of $\ddot{y}_i(t)$ from Equation (4). Back-to-back accelerometers doubled the number of acceleration ensembles used for computing spectral averages, and this reduces random errors.

$$\mathbf{A}^A_{ij}(f_k) = \frac{1}{nN\Delta t}\sum_{l=1}^{n}\sum_{\beta=1}^{2}\left[a^{\beta *}_{il}(f_k)\, a^{\beta}_{jl}(f_k)\right] \qquad i,j = 1,2,\ldots 6 \quad k = 0,1,\ldots \frac{N}{2} \tag{11}$$

$a^1_{il}(f_k)$ FFT of $\ddot{y}^1_i(t)$, block l, at frequency f_k

$a^2_{il}(f_k)$ FFT of $\ddot{y}^2_i(t)$, block l, at frequency f_k

VET mass center one-sided load spectral density functions are computed in Equation (12) for VET Configuration A. NCC emitted disturbance loads are proportional to the displacement measurement below the VET suspension frequency, and disturbances are proportional to the acceleration measurement above the suspension frequency. The proportionality functions are the stiffness tensor and mass tensor, respectively, from Equation (5), the VET system dynamic equations of motion.

$$\mathbf{F}_{ij}^{A}(f)=\begin{cases}\sum_{k=1}^{6}\sum_{l=1}^{6}K_{ik}^{A}\mathbf{D}_{kl}^{A}(f)\left(K_{jl}^{A}\right)^{T}, & f<f_s\\ \sum_{k=1}^{6}\sum_{l=1}^{6}M_{ik}^{A}\mathbf{A}_{kl}^{A}(f)\left(M_{jl}^{A}\right)^{T}, & f\geq f_s\end{cases} \quad (12)$$

$$i,j=1,2,\ldots 6$$

The final load spectral density functions are constructed by combining load spectra for VET Configurations A and B from Equation (12). Configuration A was used to compute load spectra for X1 and X2 translation and X1 and X3 rotation (degree-of-freedom indices 1, 2, 4, and 6). Configuration B was used to compute load spectra for X3 translation and X2 rotation (degree-of-freedom indices 3 and 5). These components were selected based upon the axis directions with low-frequency suspension. Cross spectral density functions are zeroed if different VET configurations contribute. Equation (13) shows the VET spectral density functions for loads acting at the VET mass center.

$$\mathbf{F}(f)=\begin{bmatrix}\mathbf{F}_{11}^{A} & \mathbf{F}_{12}^{A} & 0 & \mathbf{F}_{14}^{A} & 0 & \mathbf{F}_{16}^{A}\\ \mathbf{F}_{21}^{A} & \mathbf{F}_{22}^{A} & 0 & \mathbf{F}_{24}^{A} & 0 & \mathbf{F}_{26}^{A}\\ 0 & 0 & \mathbf{F}_{33}^{B} & 0 & \mathbf{F}_{35}^{B} & 0\\ \mathbf{F}_{41}^{A} & \mathbf{F}_{42}^{A} & 0 & \mathbf{F}_{44}^{A} & 0 & \mathbf{F}_{46}^{A}\\ 0 & 0 & \mathbf{F}_{53}^{B} & 0 & \mathbf{F}_{55}^{B} & 0\\ \mathbf{F}_{61}^{A} & \mathbf{F}_{62}^{A} & 0 & \mathbf{F}_{64}^{A} & 0 & \mathbf{F}_{66}^{A}\end{bmatrix} \quad (13)$$

HST boresight jitter is computed by multiplying the load spectral density functions by complex MIMO transfer functions from the NCC mass center input loads to the HST boresight attitude outputs. An example of one of these transfer functions is shown in Figure 1. Prior to performing this step, the load spectra in Equation (13) must be transformed from VET mass center loads to NCC mass center loads. The HST boresight jitter equation is shown in Equation (14).

$$\theta_j=\sqrt{2\Delta f\sum_{f}\sum_{i,j=1}^{2}\sum_{k,l=1}^{6}G_{ik}^{H}(f)\mathbf{F}_{kl}(f)G_{jl}(f)} \quad (14)$$

$G_{ik}(f)$ MIMO transfer functions from HST load input k at the NCC mass center to boresight component i

$G_{ik}^{H}(f)$ Conjugate transpose (Hermitian) of $G_{ik}(f)$

The load spectral density functions, Equation (13), reveal the NCC disturbance force characteristics during surging. The X1-axis force autospectra is shown in Figure 20. The fundamental surging frequency is at 3.5 Hz, and integer multiples of the surging frequency are evident up to 50 Hz.

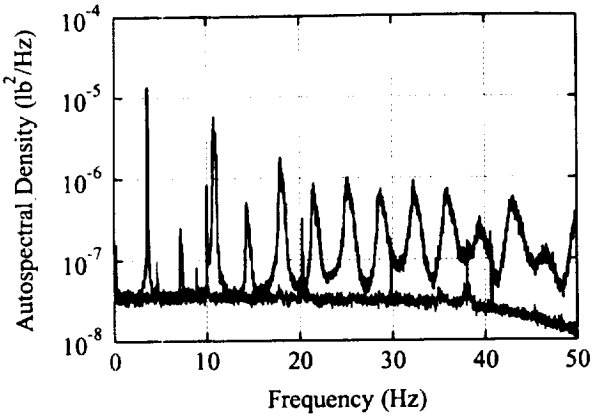

Figure 20. VET X1-axis NCC Mass Center Force Autospectra for NCC Compressor at 5800 rps (black) and NCC Off (red).

The linear analysis process described by Equations (10) through (14) was used to compute HST jitter due to NCC disturbances. A review of the results indicated that not all disturbance components were significant contributors to HST jitter. Specifically, NCC emitted forces cause at least 98% of the jitter for HST, and NCC emitted torques produce insignificant HST jitter. NCC loads that produce jitter are primarily due to VET acceleration measurements. Displacement measurements, below the VET suspension frequency, contribute only 3% of the overall HST jitter. These results suggest a simple algorithm may be used to compute NCC emitted loads: VET acceleration measurements multiplied by the VET system mass. This relationship is consistent with the acceleration-to-force relationship in Figure 16, because the frequency content of the surging disturbance (3.5 Hz and above) is well separated above the VET suspension frequency.

The linear analysis was repeated using a shorter ensemble length to increase the number of spectral averages and reduce uncertainties due to random errors from the averaging process. Because disturbances below the VET suspension frequencies were known to contribute insignificant jitter, only frequencies above 0.017 Hz were considered for these jitter computations. Results of the linear frequency-domain analysis are shown in Table 3. These results were computed using 132 spectral averages, 60-second ensembles, and no uncertainties were applied. VET RSS accelerations increase with increasing compressor speed, but HST

jitter does not follow the same trend. The lower compressor speed produces larger disturbances below 0.5 Hz, the region of greatest sensitivity for the HST attitude control law, as shown in Figure 1. Hence, HST jitter is higher for the lower compressor speed.

VET Measurement	NCC CM RSS Acceleration (micro-g)	HST Boresight Jitter (mas)
NCC Off Background	20	3.2
NCC 5800 rps Compressor	34	3.6
NCC 6500 rps Compressor	35	3.4

Table 3. Linear Frequency-Domain Analysis Results (60 second rms values)

Although NCC emitted disturbances have a broad range of spectral content (Figure 20), the HST jitter caused by structural mode excitation was insignificant. HST has numerous structural modes above 1 Hz, as shown in Figure 1, and several were excited by the NCC surging harmonics, but these responses did not dominate the HST jitter response. Results in Table 3 indicate that the VET background noise was the primary contributor to HST jitter, and this emphasizes the importance of using a quiet facility for disturbance testing of HST components.

An elementary uncertainty analysis was performed for the frequency-domain process to bound the errors in the HST jitter estimates. The largest systematic errors were a 5% (2σ) error in VET mass properties and sensor mounting locations and a 10% (2σ) error in the HST structural dynamic model. The RSS systematic error was 11% (2σ). The normalized 2-sigma random error due to spectral averaging, Equation (15), is a function of the number of ensembles, n, used in the averaging process. Using 132 ensembles for final jitter computations, the random error is 17% (2σ).

$$\varepsilon_{ran} = \frac{2}{\sqrt{n}} \tag{15}$$

The overall uncertainty is the RSS of the random and systematic errors.[6] The uncertainty in HST jitter computations from VET measurements is 20% (2σ). Therefore, the linear analysis estimate for HST jitter is 3.6 ± 0.7 mas rms with 95% confidence.

NON-LINEAR TIME-DOMAIN ANALYSIS

The HST Pointing Control System simulation, HSTSIM, was used for the non-linear time-domain analysis. The simulation was developed prior to HST launch in 1990, and it is maintained to match the changing on-orbit characteristics of the observatory. HSTSIM is a high-fidelity non-linear time domain simulation used to predict HST pointing performance during normal operating modes. It contains linear and non-linear structural dynamic models of the HST, it models all actuators and sensors, including reaction wheels, rate gyros, and Fine Guidance Sensors, and it models all non-linear characteristics of the attitude control law. HSTSIM includes an orbit dynamics model, magnetic field model, a spherically aberrated star model, and all environmental disturbance sources significant to HST. The simulation also includes up-to-date flight software used onboard the HST flight computer. HSTSIM has been used successfully in the design process for control law modifications necessary to attenuate undesirable jitter and prevent guide star loss-of-lock due to solar array disturbances.

The NCC VET disturbance was added to HSTSIM and used for high-fidelity prediction of HST on-orbit performance after SM3B. The time domain disturbance was computed using Equation (16), again acknowledging the insignificance of VET displacement measurements in jitter-producing loads.

$$F_i(t) = \begin{cases} \sum_{j=1}^{6} M_{ij}^{A} \ddot{y}_j^{A1} , & i = 1,2,4,6 \\ \sum_{j=1}^{6} M_{ij}^{B} \ddot{y}_j^{B1} , & i = 3,5 \end{cases} \tag{16}$$

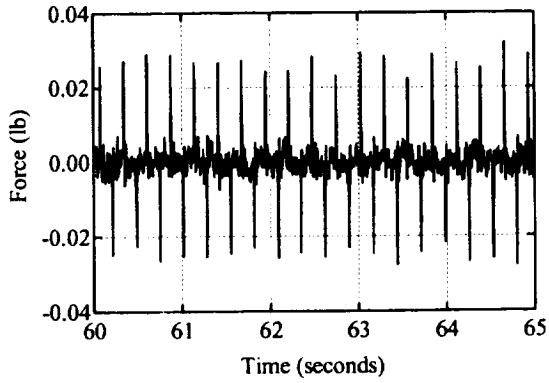

Figure 21. VET X1-axis NCC Mass Center Force for NCC Compressor at 5800 rps.

This equation describes time-domain forces acting at the VET mass center. An additional transformation is required to transform these loads to the NCC mass center. Data from both VET configurations in Equations (4) and (5) are used to compute Equation (16). A five-second segment of the VET X1-force time response is shown in Figure 21.

HSTSIM predictions for HST on-orbit jitter after SM3B with all disturbance sources active indicate the NCC is the only disturbance source that produces significant jitter for HST. HSTSIM predicts 3.1 mas HST jitter (60 second rms) during NCC surging at 5800 rps, and with the NCC disturbance removed, HSTSIM predicts 2.3 mas rms, the rate gyro noise floor. These jitter predictions meet the original Pointing Control Jitter Budget level of 3.2 mas rms overall HST jitter after SM3B, and the jitter prediction is within the 7 mas rms HST mission requirement. HSTSIM predictions were also within the error bound of the HST jitter prediction using the linear frequency-domain analysis method. The Vehicle Disturbance Test, a mandatory activity during the Servicing Mission Orbital Verification period, after SM3B, will measure actual HST on-orbit jitter during NCC surging and steady state operation.

CONCLUSION

The Vibration Emittance Test was a state-of-the-art ground test that measured NICMOS Cryogenic Cooler surging disturbances at or below the stringent on-orbit disturbance levels for the Hubble Space Telescope. Measurements acquired during the VET were analyzed using linear frequency-domain and non-linear time-domain methods to quantify NCC disturbances and predict HST on-orbit jitter. These analyses predict HST compliance with the 7 milli-arcsecond rms pointing stability requirement after installation of the NICMOS Cooling System. Upper-bound HST jitter during NCC surging is predicted to be 3.1 milli-arcseconds (60 second rms), and after NICMOS cooldown, HST jitter is predicted to be 2.3 milli-arcseconds rms. The VET noise floor RSS acceleration was 20 micro-g rms, and a RSS acceleration of 35 micro-g rms was measured with the NCC running. The NCC surging disturbance exhibits spectral content at the 3.5 Hz surging frequency and at integer multiples of the surging frequency. HST jitter due to structural excitation at these frequencies was insignificant. VET background noise was the primary contributor to HST jitter, emphasizing the importance of selecting a quiet facility for disturbance testing of HST components.

ACKNOWLEDGEMENTS

The authors acknowledge the contributions of Mr. Mark Turczyn for his support of this test and analysis effort. This work was performed for the NASA Goddard Space Flight Center under contract NAS5-50000.

REFERENCES

1. Story, D., Cofie, E., Clapp, B., Cepollina, F., Of the NASA Hubble Space Telescope (HST) Near Infrared Camera Multi-Object Spectrometer (NICMOS) Cryogenic Cooler (NCC) in a Microgravity Environment. 52nd International Astronautical Congress, Toulouse, France, October 2001.

2. Jedrich, N., Zimbelman, D., Turczyn, M., Sills, J., Voorhees, C., Clapp, B., Cryo Cooler Induced Micro-Vibration Disturbances to the Hubble Space Telescope. Cranfield University 5th International Conference on Dynamics and Control of Systems and Structures in Space, Cambridge, England. To be published in July 2002.

3. Voorhees, Carl R., Sills Jr., Joel W., Clapp, Brian, A System for Microgravity Measurements on the HST NCC Vib Emittance Test. 71st Shock and Vibration Symposium, SAVIAC, November 2000.

4. Sills Jr, J. W., Voorhees, C. R., Characterization and Application of Pneumatic Suspension Devices for Vibration Disturbance Testing. 20th International Modal Analysis Conference, IMAC, February 2002.

5. Bendat, Julius S., and Piersol, Allan G., Random Data: Analysis and Measurement Procedures, Second Edition (Revised and Expanded). New York, John Wiley & Sons, 1986.

6. Taylor, John R., An Introduction to Error Analysis: The Study of Uncertainties in Physical Measurements, Second Edition. Sausalito, California, University Science Books, 1997.